SPE11

Convergence Study and Extension to Realistic Physics

Hadjisotiriou, G.; Sass, J.; Wapperom, M.; Novikov, A.; Voskov, D. V.

DOI
10.2118/223922-MS

Publication date
2025

Document Version
Final published version

Published in
Society of Petroleum Engineers - SPE Reservoir Simulation Conference, RSC 2025

Society of Petroleum Engineers

SPE-223922-MS

SPE11: Convergence Study and Extension to Realistic Physics

G. Hadjisotiriou, TU Delft; J. Sass, Equinor; M. Wapperom and A. Novikov, TU Delft; D. V. Voskov, TU Delft, Stanford University

Abstract

The SPE11 comparative solution project presents a benchmark for geological carbon storage in an aquifer, as the development of sufficiently accurate CO_2 sequestration models is critical for predicting the distribution of CO_2 during and after injection. In this paper we present a convergence analysis of the SPE11 benchmark simulation using the Delft Advanced Research Terra Simulator (open-DARTS). Open-DARTS, an open-source simulation framework designed for forward and inverse modeling, as well as uncertainty quantification, employs a unified thermal-compositional formulation and operator-based linearization. In our convergence analysis the SPE11b (2D - reservoir conditions) starts to converge at a grid resolution of 1340 × 240, after which added resolution provides diminishing returns. In addition the three-dimensional SPE11c benchmark is simulated with *8M* grid blocks. However, 2D results from SPE11b suggest that a greater resolution is required for a truly converged solution. Furthermore, we extend the SPE11b benchmark to include H_2S as a trace impurity in the injection stream.

Introduction

During geological carbon sequestration (GCS), CO_2 is captured from industrial point sources, transported and injected into geological formations. To ensure permanent storage, these geological storage complexes must comprise a combination of permeable reservoirs and impermeable sealing units. Therefore, saline aquifers and depleted oil and gas reservoirs are considered suitable for GCS. Deep saline aquifers have the advantage of offering the largest proven volumes for CO2 storage, whereas depleted hydrocarbon reservoirs demonstrate a proven ability to store buoyant fluids, are well-characterized, and have existing infrastructure in place (Ringrose, 2020).

Once injected, CO_2 is trapped through a combination of various trapping mechanisms, including structural, residual and solubility trapping. In the shorter time scale, structural and residual trapping mechanisms are expected to dominate, while dissolution trapping occurs over longer time scales (Metz et al., 2005). During structural trapping, the injected CO_2 accumulates under a capillary barrier or impermeable sealing layer. Residual trapping occurs when the CO_2 plume migrates due to buoyancy. In this process, CO_2 at the tail of the plume is immobilized at the pore scale during CO_2 drainage when the wetting phase is imbibed back into the pore space (Krevor et al., 2015). At this point, the CO_2 exists as a series of disconnected

ganglia separated by water. During solubility trapping, CO_2 dissolves into the aquifer water. This molecular diffusion process occurs slowly and is enhanced by the convective mixing of the brine and CO_2 (Neufeld et al., 2010). Convective mixing starts at the interface between CO_2 and water. As CO_2 dissolves into the brine, density-driven flow is induced which in turn increases the dissolution rate. To accurately model this process, high-fidelity models are run for large time spans, as the onset of convective mixing can occur over tens to thousands of years (Pruess and Nordbotten, 2011; Riaz et al., 2006; Pau et al., 2010). CO_2 dissolution is one of the primary mechanisms with which CO_2 will be permanently and safely stored in the subsurface in the long term.

Previous intercomparisons by Pruess et al. (2004) have shown a good agreement between solutions obtained with different numerical simulators. The authors attribute discrepancies to differences in the descriptions of fluid properties. However, convective dissolution always introduces a significant challenge to the modeling of long-term CO_2 sequestration at the reservoir scale. Elenius et al. (2015) present for the first time a numerically converged solution for a large-scale plume migration problem encompassing a wide range of dominant physical phenomena, including enhanced CO_2 dissolution. The first benchmark study fully linking experiments and simulations of enhanced dissolution processed was proposed by Nordbotten et al. (2022). A representative heterogeneous geometry based on typical North Sea reservoirs was constructed in a meter-scale rig, filled with unconsolidated sands of different types. The forecasts reported by different numerical simulation groups were analyzed in the presence of physical ground truth, provided by a series of repeated experiments on the experimental rig (Flemisch et al., 2024). Several advanced methodologies including data assimilation based on tracer test results (Tian et al., 2024) and the use of Multi-Point Flux Approximation (Wapperom et al., 2024) were reported as the result of this benchmark study.

The SPE11 comparative solution project (CSP) borrows its geometry from the FluidFlower experiment and offers a baseline for simulation of CO_2 storage in aquifers (Nordbotten et al., 2024). The reservoir is a heterogeneous reservoir storage complex resembling those found on the Norwegian continental shelf. Three versions of the benchmark are presented in the CSP. The first, 11a is a 2D lab-scale geometry at surface conditions. The second, 11b, is geometrically identical to 11a but at reservoir scale and conditions. The third and last, 11c, is a 3D extruded version of 11b that includes an anticline. The aim of the CSP is to provide a reference case for the development of numerical simulation of GCS by comparative study. The SPE11 CSP explicitly specifies all reservoir and fluid properties in Nordbotten et al. (2024). In this study, the convergence analysis of the SPE11 benchmark simulation utilizing the Delft Advanced Research Terra Simulator (DARTS) is presented. Furthermore, the original physics of the benchmark is extended to include impurities in the CO_2 injection stream. This follows the experience with the largest and longest running CO_2 storage projects where trace amounts of other gasses, such as H_2S and CH_4, are injected. In the case of the Sleipner field, CO_2 is injected with a 0.5 — 2% fraction of methane (Eiken et al., 2011) and hydrogen sulfide is injected with CO_2 in the case of the Weyburn project (Whittaker et al., 2004).

Planning CO_2 storage projects requires developing an understanding of the storage conditions, and fluid flow behavior. To this extent, reservoir simulation is used to predict the migration of CO_2 pressure and storage capacity of the reservoir. Accurate modeling of CO_2 sequestration necessitates the inclusion of complex physical processes, including gravity, capillarity, diffusion, mechanical dispersion, and multiphase flow. To accurately capture the effect of dissolution trapping, it is necessary to solve the highly nonlinear, coupled system of equations, accounting for all these effects, with sufficient resolution and over extended timescale. This study utilizes open-DARTS, an open-source simulation framework designed for forward and inverse modeling, as well as uncertainty quantification (Voskov et al., 2024). Open-DARTS employs a unified thermal-compositional formulation and operator-based linearization (Voskov, 2017). This approach allows users to easily adjust the terms of the PDEs and model various complex physical phenomena. Additionally, open-DARTS leverages GPU paralleliza-tion, enabling simulations to run close to an order of magnitude faster compared to CPU implementation (Khait and Voskov, 2021).

In this study, we begin with a brief description of governing equations, thermodynamic properties, reservoir description and boundary conditions for SPE11 benchmark. Next, we present a convergence study for SPE11b reservoir, followed by a comparison of the converged solution with the results of the high-resolution SPE11c simulation. Subsequently, we present the results of the more realistic version of the SPE11b model, which includes typical impurities in the CO_2 stream. Finally, we conclude this study with lessons learned and suggestions for future work.

The SPE11 - Comparitive Solution Project

What follows is an abbreviated description of the SPE11 comparative solution project. For a complete description of the CSP please refer to the official technical description by Nordbotten et al. (2024). As CO_2 is frequently injected at lower temperatures than the reservoir a thermo-compositional formulation is used. In DARTS the advective-diffusive multiphase multicomponent formulation is used (Lyu and Voskov, 2023). The mass conservation equation for component c is written as,

$$\frac{\partial}{\partial t}\left(\phi \sum_{j=1}^{np} \rho_j s_j x_{cj}\right) + \nabla \cdot \left(\sum_{j=1}^{np} x_{cj} \rho_j \boldsymbol{u}_j + \mathbf{J}_{cj}\right) = 0, \quad c = 1, \ldots, n_c, \tag{1}$$

where ϕ is porosity, S_j is phase saturation, ρ_j is molar phase density and x_{cj} is molar fraction of component c in phase j. Additionally, the thermal equation for multiphase flow accounts accounts for advective and conductive heat flow and contains contributions from both fluid and rock,

$$\frac{\partial}{\partial t}\left(\phi \sum_{j=1}^{np} \rho_j s_j U_j + (1-\phi) U_r\right) + \nabla \cdot \left(\sum_{j=1}^{np} h_j \rho_j \boldsymbol{u}_j + \kappa \nabla T\right) = 0, \tag{2}$$

where U_j is specific internal energy of phase j, U_r is rock specific internal energy and κ is effective heat conductivity. The phase velocity $\boldsymbol{u}_j$ follows Darcy's law for multiphase flow,

$$\boldsymbol{u}_j = -\mathbf{K}\frac{k_{rj}}{\mu_j}\left(\nabla p_j - \rho_j g \nabla z\right), \tag{3}$$

where $\mathbf{K}$ is the permeability tensor, k_{rj} is relative phase permeability, μ_j is phase viscosity, p_j is phase pressure, g is gravitational acceleration, and z is depth. The diffusive flux $\mathbf{J}_{cj}$ of component c in phase j is described by Fick's law as

$$\mathbf{J}_{cj} = -\left(\phi s_j D_{cj} + E|\mathbf{u}_j|\right)\nabla\left(\rho_j x_{cj}\right), \tag{4}$$

where D_{cj} is diffusion coefficient of component c in phase j, E is dispersivity coefficient, equal for all components in all phases. This formulation accounts for the dispersion term, scaled by the scalar dispersivity coefficient and the magnitude of Darcy's velocity. The velocity vector is reconstructed at cell centers using a least-squares solution of fluxes across all cell's interfaces, then averaged between neighboring cells and explicitly incorporated into the numerical approximation of the dispersion term. This system of equations is closed by capillary, thermal and thermodynamic equilibrium assumptions.

Thermodynamics and physical properties

A negative flash procedure with successive substitution is employed for resolving thermodynamic equilibrium calculations (Michelsen, 1982; Whitson and Michelsen, 1989). The fugacities of the vapor phase are evaluated using a cubic equation of state (Peng and Robinson, 1976) and the fugacities of the water phase are calculated using an activity model based on Henry's constants (Ziabakhsh-Ganji and Kooi, 2012). Using this hybrid-model approach, the implementation of a separate model for the aqueous phase

maintains the simplicity of solving phase equilibrium problems with cubic equations of state while obtaining an accurate thermodynamic description of the aqueous phase (Wapperom et al., 2025).

The property correlations for SPE11 and open-DARTS are presented in Tab. 1. The properties of pure phases of the SPE11 CSP are defined in accordance with the NIST database (Lemmon et al., 2023). Wapperom et al. (2024) compared the results of our modelling approach with those of NIST and found good agreement. Fig. 1 presents the results of DARTS, verified against various data sets available in the literature. The considered properties are highly dependent on pressure and temperature, with the exception of the dissolved H_2O in the CO_2-rich phase at field conditions. At elevated pressures, changes in pressure exert minimal influence on solubility when the CO_2 is in a dense phase. Conversely, at low pressures, CO_2 in a vaporous state results in a greater concentration of H_2O within the CO_2 phase. As pressure decreases, the transition from the vapor phase to the dense phase gives rise to a pronounced decline in solubility.

Table 1—Fluid properties of 11b and 11c

Properties	SPE11	open-DARTS
CO_2 density, kg/m^3	Lemmon et al. (2023)	Peng and Robinson (1976)
H_2O density, kg/m^3	Garcia (2001)	
CO_2 viscosity, cP	Lemmon et al. (2023)	Fenghour et al. (1998)
H_2O viscosity, cP	Lemmon et al. (2023)	Islam and Carlson (2012)
CO_2 enthalpy, kJkmol^{-1}	Lemmon et al. (2023)	Peng and Robinson (1976)
H_2O enthalpy, kJkmol^{-1}	Lemmon et al. (2023)	Ziabakhsh-Ganji and Kooi (2012)
Mutual solubilities	Spycher et al. (2003)	Wapperom et al. (2025)
Gas diffusion coefficient, m^2/s	2×10^{-8}	
Water diffusion coefficient, m^2/s	1×10^{-9}	

Table 2—Porous media properties

Properties	Values
Dispersivity, E	10
Immobile gas saturation, $s_{n,imm}$	0.1
Max capillary pressure, $p_{cap,\,max}$, Pa	3×10^7
Shape exponent capillary pressure, c_2	1.5
Rock specific heat capacity, C_s, kJkg^{-1} K^{-1}	8.5×10^{-1}
Rock density, ρ_s, kgm^{-3}	2500
Shape exponents rel.ative permeability, $c_{\alpha,1}$	1.5
Normalized saturations, $s_{j,n}$	$\max\frac{s_j - s_{j,imm}}{1 - s_{j,imm}}$
Relative permeability, k_{rj}	$\left(s_{j,n}\right)^{c\alpha,1}$
Entry pressure, p_{entry}, bar	$\sqrt{\phi / k_x}\, 6.12 \times 10^{-3} Nm^{-1}$

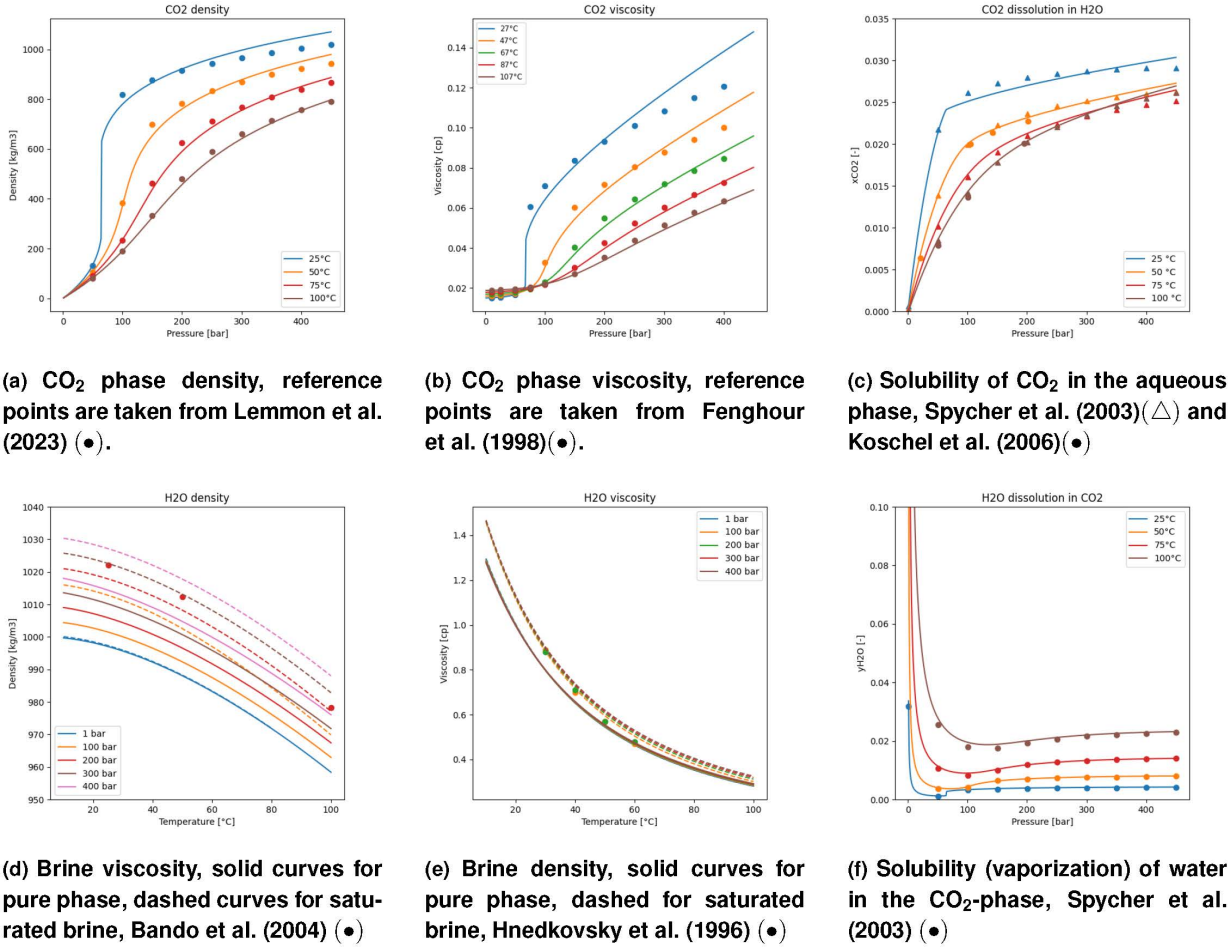

(a) CO_2 phase density, reference points are taken from Lemmon et al. (2023) (•).

(b) CO_2 phase viscosity, reference points are taken from Fenghour et al. (1998)(•).

(c) Solubility of CO_2 in the aqueous phase, Spycher et al. (2003)(△) and Koschel et al. (2006)(•)

(d) Brine viscosity, solid curves for pure phase, dashed curves for saturated brine, Bando et al. (2004) (•)

(e) Brine density, solid curves for pure phase, dashed for saturated brine, Hnedkovsky et al. (1996) (•)

(f) Solubility (vaporization) of water in the CO_2-phase, Spycher et al. (2003) (•)

Figure 1—Fluid properties computed in this work.

In addition, the capillary pressure p_c, defining pressure drop between wetting and non-wetting phases, is governed by the following relationship

$$p_c(s_w) = \mathrm{p}_{\mathrm{cap,max}} \cdot \mathrm{erf}\left(\left(\mathrm{p}_{\mathrm{entry}}(s_{\mathrm{w,n}})^{-1/\mathrm{c}_2} / \mathrm{p}_{\mathrm{cap,max}}\right)(\sqrt{\pi}/2)\right), \quad (5)$$

where $\mathrm{p}_{\mathrm{cap,\,max}}$ is maximum capillary pressure, $\mathrm{p}_{\mathrm{entry}}$ is entry pressure, c_2 is empirical parameter. The exact values of these properties are provided in Tab. 2.

Reservoir

Seven different facies are defined in both the 11b and 11c reservoir models. Facies 1 represents the storage complex and serves as a capillary barrier to migrating CO_2. Facies 2 through 5 consist of permeable reservoir sands, while Facies 6 corresponds to fault infill. Finally, Facies 7 forms an impermeable barrier. The facies distribution is shown in Fig. 2 for 11b model. The 11c model is an extruded version of the 11b model and, in addition, it includes anticline. Note that in SPE11, the reservoir geometry defines the z-axis at the base of the reservoir. Facies properties are identical for both models and are listed in Tab. 3. The vertical permeability of each of the facies is one-tenth of its horizontal permeability. Model geometries of the three SPE11 variants are hosted on the GitHub repository: https://github.com/Simulation-Benchmarks/11thSPE-CSP. Reservoir geometries are provided in the GMSH geometry format and available in the SPE11 repository. In our model, the geometry of the FluidFlower model is converted to the reservoir scale following the SPE11's description. For all simulations, a structured mesh is constructed and populated according to the facies descriptions.

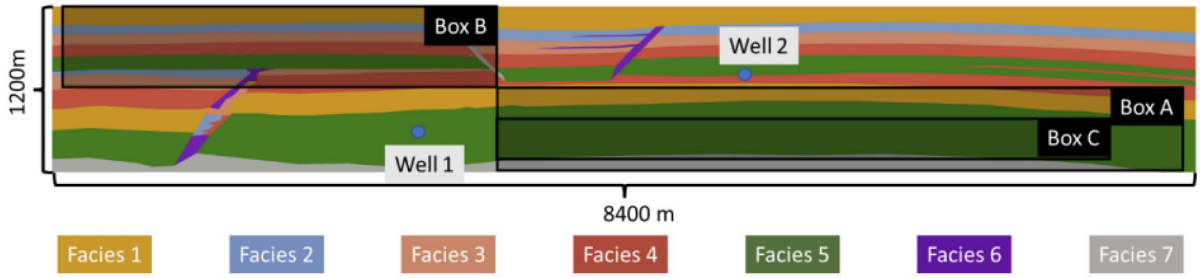

Figure 2—11b reservoir with corresponding reporting boxes and well locations. Image from Nordbotten et al. (2024).

Table 3—Facies properties of 11b and c.

Facies no.	Permeability k, mD	Porosity ϕ	$s_{w,\mathrm{imm}}$	κ_s, $\mathrm{Wm^{-1}\,K^{-1}}$
1	0.101	0.10	0.32	1.90
2	101	0.20	0.14	1.25
3	202	0.20	0.12	1.25
4	507	0.20	0.12	1.25
5	1013	0.20	0.12	0.92
6	2027	0.25	0.12	0.26
7	0	0	0.10	2.00

Initial/boundary conditions

In the SPE11b and 11c models, temperatures at the top and bottom boundaries are fixed, all boundaries are impermeable and the boundary volumes are increased to $5 \times 10^4 \Delta z$. No CO_2 is present in the system prior to injection. A geothermal gradient of 25 °Ckm^{-1} is applied along with a temperature of 70 °C maintained at the bottom boundary. The initial reservoir pressure is hydrostatic and defined as,

$$p_{w,\,initial} = 3 \times 10^{-7}\ \mathrm{Pa} - g\int_{300\ \mathrm{m}}^{z} \rho_w(p, T)dz, \tag{6}$$

where ρ_w is water phase density. The model undergoes an equilibration step lasting 1000 yr prior to injection, with t = 0yr defined as the start of injection. Both the 11b and 11c models include two injection wells. In model 11b, well 1 is located at (2700, 300), and well 2 at (5100, 1100). For model 11c, well 1 is horizontal, it perforates reservoir between points (2700, 1000, 300) and (2700, 4000, 300). Well 2 perforates reservoir between points (5100, 1000, 700) and (5100, 4000, 700). In both models injection starts in well 1 at t = 0yr and continues until t = 50 yr. Well 2 starts injection at t = 25 yr, lasting until t = 50yr. In the post-injection period, the simulation continues until t = 1000 yr. In both wells, CO_2 is injected at 10 °C. In 11b the injection rate is equal to 3024kgd^{-1} and in 11c 50kgs^{-1}.

Solution strategy

A finite-volume discretization is employed, using the backward-Euler scheme in time and two-point flux approximation with upstream weighting in space. Operator-based linearization (OBL) is used to manage the computational cost of property evaluation and Jacobian assembly. In OBL, the governing equations are represented through state-dependent and spatial operators. State-dependent operators aggregate variables that depend on the physical state into a single term, i.e. operator. The state-operators are resolved on a uniform mesh introduced in the physical space. While the operators undergo exact evaluation at the nodes of this mesh, multilinear interpolation ensures a continuous representation of the operators between the nodes. The mesh resolution provides a key control over the nonlinearity of the problem, simulation performance,

and robustness of the simulation (Khait and Voskov, 2017). Therefore, to accurately capture multiphase flow in the presence of capillarity and buoyancy a resolution of 100 points is used for pressure and 1000 points for composition space (Lyu et al., 2021).

Results

Time series and spatial data are used for the SPE11 CSP. The spatial maps are shown in their native resolution and are not projected to the SPE11 reporting grid. Time series values include: pressure at two observation points (S1) and (S2), convective mixing M in box C and mass of CO_2. The mass of CO_2 contained in boxes A and B as well as in the seals is reported. The location of the boxes with respect to the injection wells is visualized in Fig. 2. Convective mixing is quantified by the following integral

$$M = \int \nabla \left| \frac{X^w_{CO2}}{X^w_{CO2,\max}} \right| dV, \tag{7}$$

where x^w_{CO2} is the mass fraction of CO_2 in water and $x^w_{CO2,\max}$ the solubility limit of CO_2 in water.

SPE11b

This study compares the simulation results of the SPE11b model obtained with various grid resolutions on a structured grid. The exact grid specifications are reported in Tab. 4. The models with 50 and 100 thousand grid blocks are considered low-resolution, whereas the models with 300 and 600 thousand grid blocks are highresolution models. The spatial solutions are shown in Figs. 3 and 4. Injection starts in well 1. Initially, the lower temperature of the injected CO_2 causes it to sink downward due to its higher density compared to the surrounding reservoir water. However, as the CO_2 equilibrates with the reservoir temperature, it migrates upwards due to buoyancy. From there, the majority of CO_2 migrates along the bottom of the overlying capillary barrier, while a portion migrates via the adjacent fault to the upper sand units.

Table 4—Grid specifications

No. grid blocks	$n_x \times n_z$	dx × dz	Runtime (GPU)
52, 500	525 × 100	16*m* × 12*m*	1h
100, 800	840 × 120	10*m* × 10*m*	2h
321, 600	1340 × 240	6.27*m* × 5*m*	7h
604, 800	1680 × 360	5.0*m* × 3.3*m*	11h

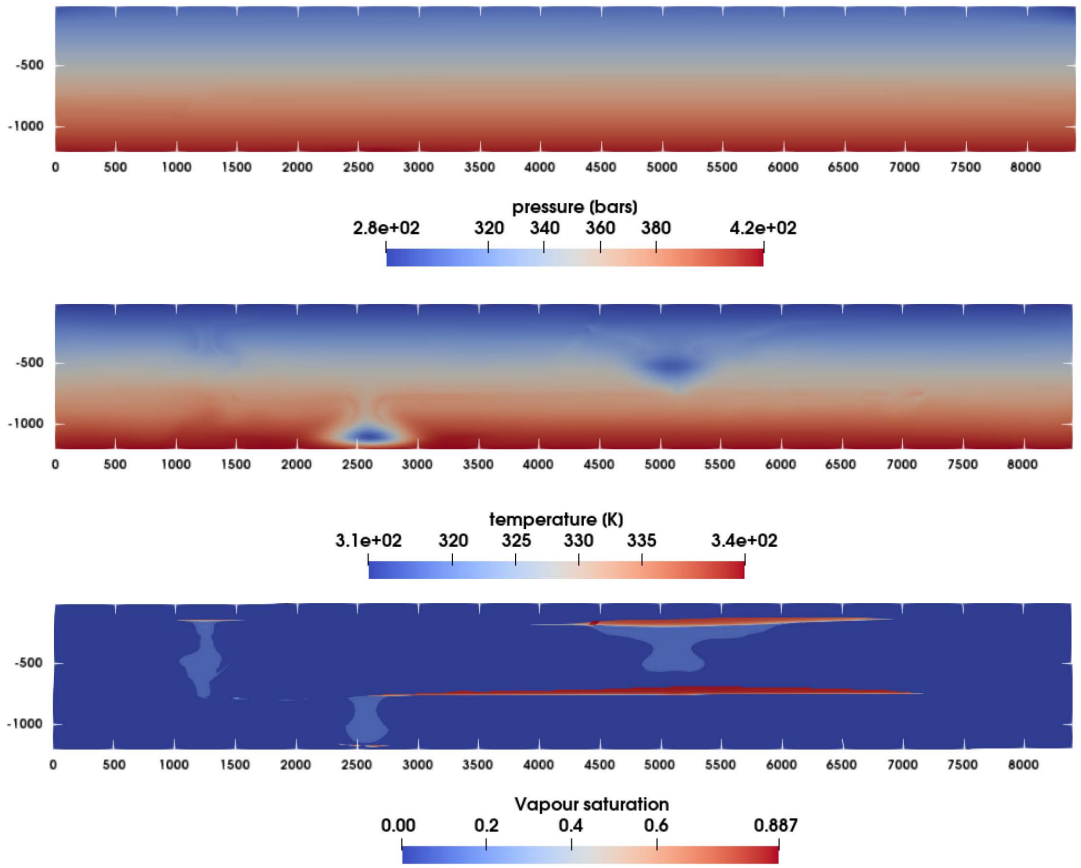

Figure 3—Pressure, temperature and gas saturation at year 300; the model has a resolution of 600K grid blocks.

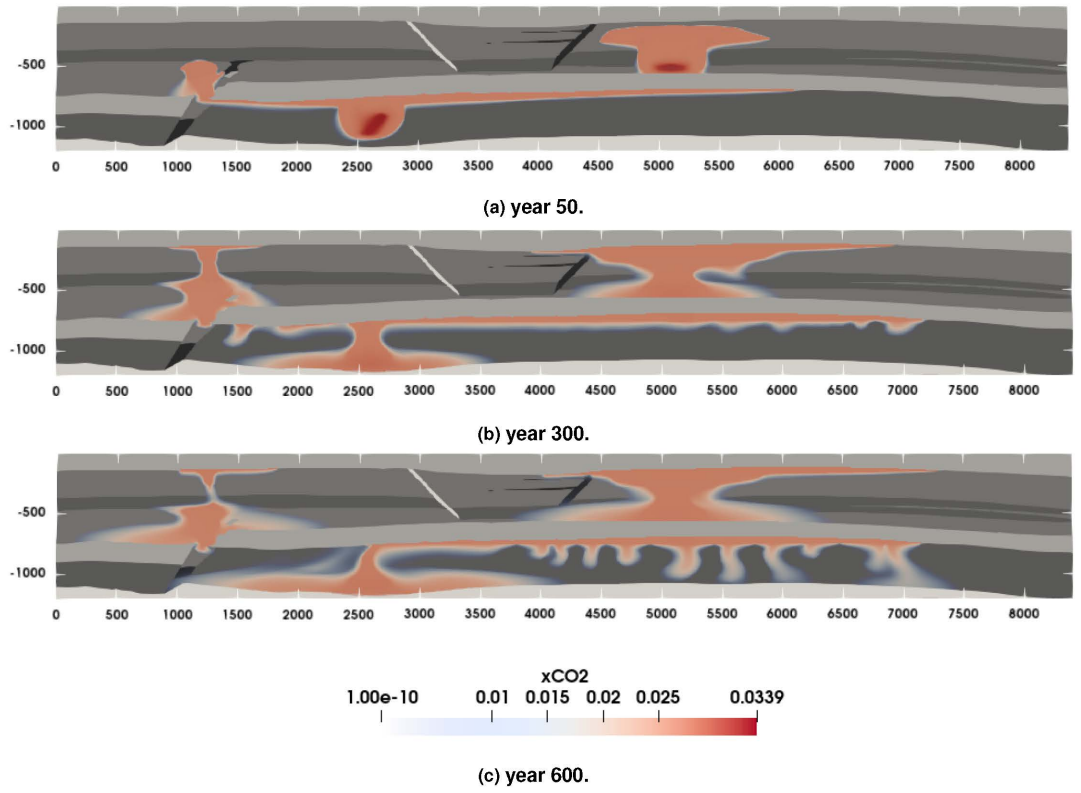

(a) year 50.

(b) year 300.

(c) year 600.

Figure 4—CO_2 fraction in liquid phase; the model has a resolution of 600K grid blocks.

As the CO_2 plume migrates upwards to box B, residual trapping takes place. In box A, two principal processes are observed: first, the CO_2 diffuses into the capillary barrier; second, the CO_2 starts to dissolve into the reservoir water. This dissolution alters the water's density, making it heavier, inducing instabilities, and leading to the formation of dissolution fingers—narrow, finger-like patterns of CO_2-saturated water. These fingers enhance the dissolution process by increasing the surface area for interaction between CO_2 and water, thereby accelerating mixing and promoting the permanent storage of CO_2.

Several observations can be derived from Fig. 5. Convective mixing increases as CO_2 dissolves into the aquifer water. The onset of dissolution can be identified as an inflection point in the curve for convective mixing and occurs in year 300. By year 600, the amount of convective mixing decreases as the more of the water column is in contact with CO_2 and density contrasts decrease. Post-injection CO_2 begins to diffuse into the sealing unit at an increasing rate.

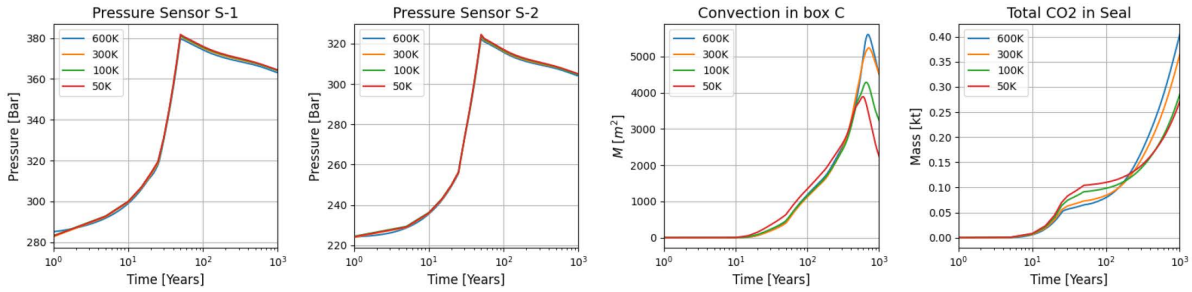

Figure 5—SPE11b time series data.

In box A, Fig. 6, minor differences are observed in the amounts of dissolved and mobile CO_2 across varying resolutions. Around year 300, the amount of mobile CO_2 begins decreasing, coinciding with the onset of enhanced dissolution and an increased dissolution rate. Nevertheless, the higher-resolution models exhibit a lower quantity of immobilized CO_2 compared to the lower-resolution models. Furthermore, the final amount of CO_2 accumulating in the seal increases with finer resolution.

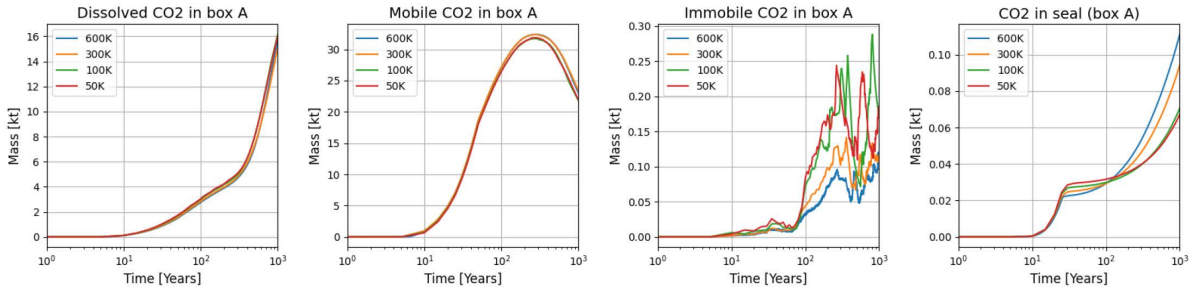

Figure 6—SPE11b, box A - bottom left (3300, 0), top right (8300, 600).

CO_2 enters the box B at approximately year 20. In box B, Fig. 7, the amount of mobile CO_2 consistently increases with finer resolutions, whereas it remains virtually unchanged for the 300 and 600 thousand grid block models. Similarly, the higher-resolution models also exhibit greater amounts of CO_2 in seal B and higher levels of dissolved CO_2, indicating a strong resolution-dependent trend across all models. No density-driven fingering is observed in box B, and greater amounts of CO_2 are immobilized compared to box A. Therefore, residual trapping is identified as the dominant trapping mechanism in box B, while solubility trapping dominates in box A.

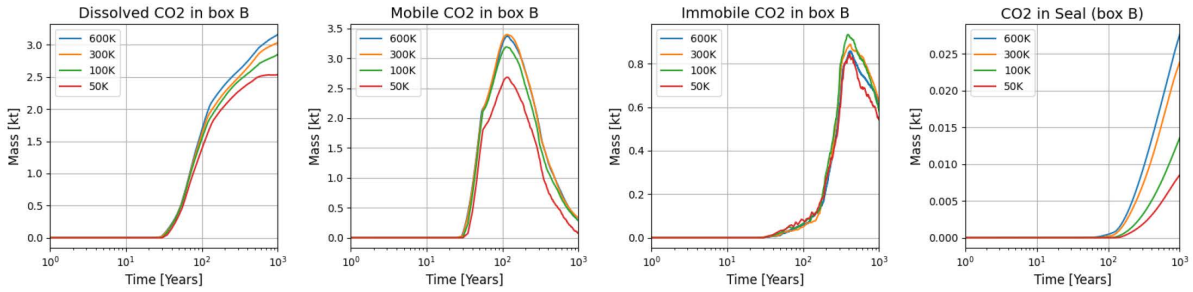

Figure 7—SPE11b, box B - bottom left (100, 600), top right (3300, 1200).

SPE11c

In addition, the full SPE11c model is run using the GPU version of DARTS. The model consists of nx = 840, ny = 250, nz = 120 blocks per dimension, corresponding to 8, 041, 864 active reservoir blocks. The 3D representation with two profiles across the model at x = 2700 and x = 6000 are shown in Fig. 8, depicting the fraction of CO_2 in liquid phase at 600 years of simulation. The results at three different time steps for cross-sections along the model at y = 2600 are presented in Fig. 9.

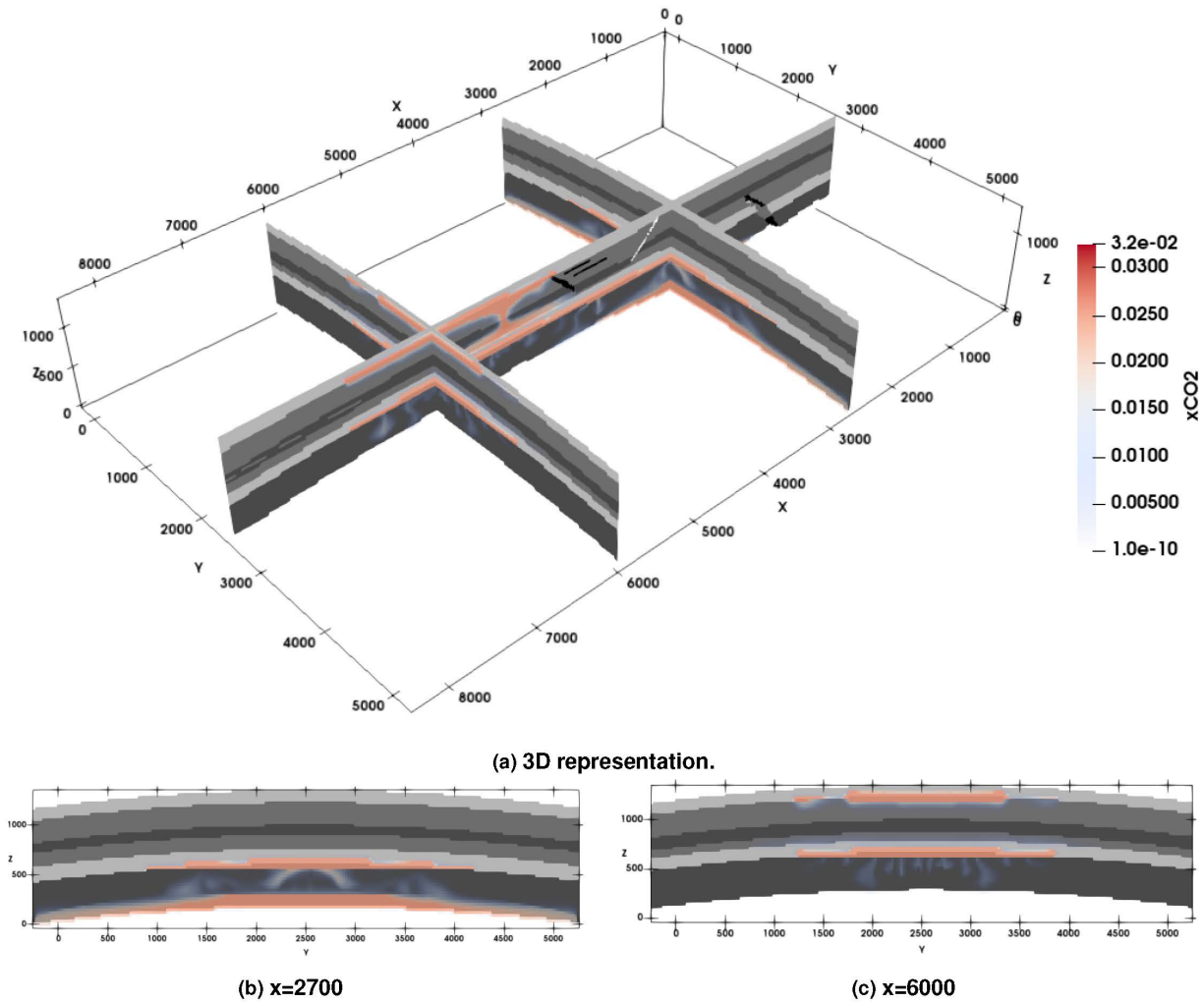

(a) 3D representation.

(b) x=2700

(c) x=6000

Figure 8—8M grid block model at year 600 with two cross-section across the model.

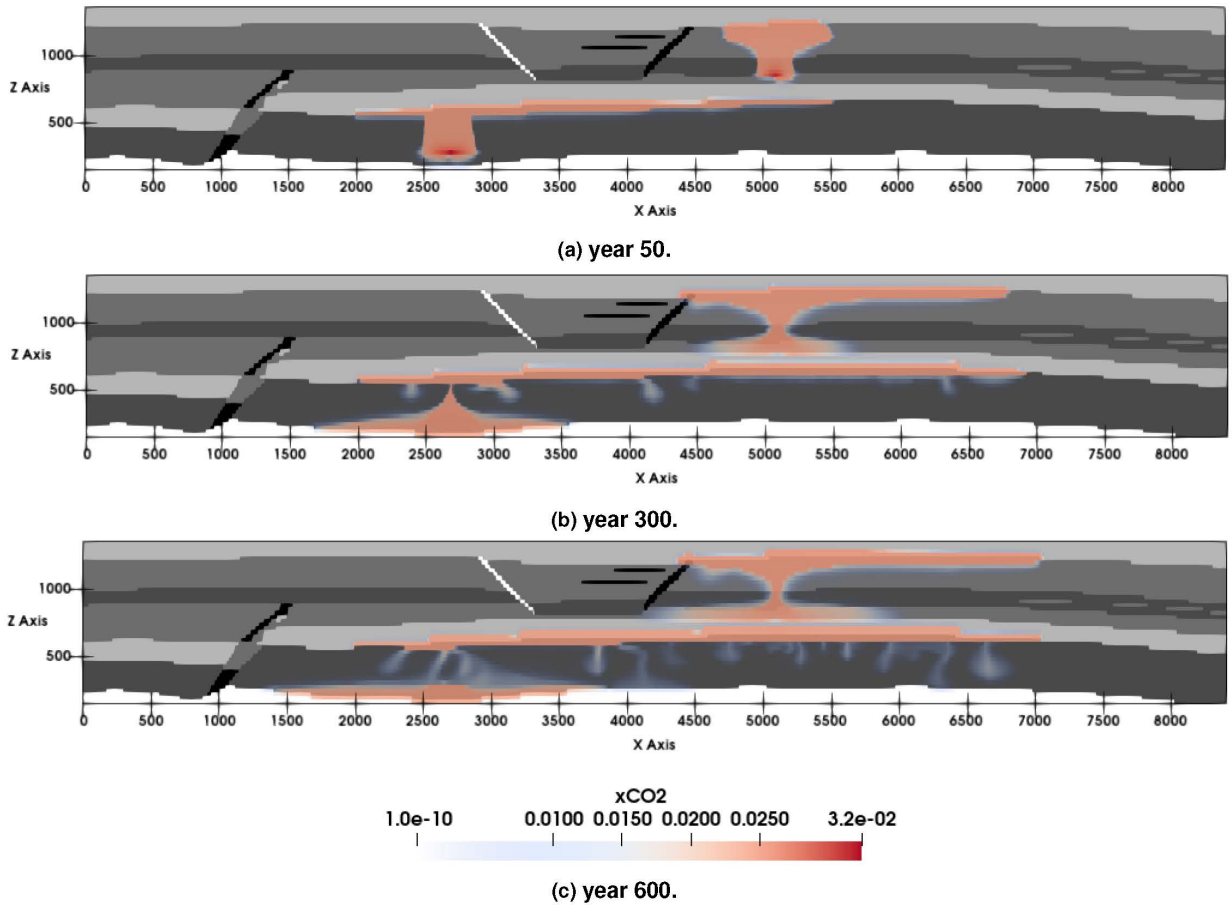

Figure 9—CO_2 fraction in liquid phase - of the SPE11c model at y = 2600.

Several differences can be derived from the comparison of Fig. 4 and Fig. 9. First, the results indicate that CO_2 does not spill through the left-most fault, which is attributed to the dipping of the reservoir. Moreover, it is quite obvious that the current resolution of the SPE11c model is insufficient to accurately capture the dynamics of enhanced dissolution, as the simulation does not resolve the characteristic length of fingers and their general dynamics.

SPE11b with impurities

In this section, we study the effect of impurities included in the injection stream of the SPE11b benchmark. There is relatively little experimental data available of H_2S-CO_2 systems at reservoir conditions. However, the experimental data show that the solubility of CO_2 decreases in the presence of H_2S (Savary et al., 2012). Field observations, experiments (Bachu and Bennion, 2009) and numerical simulations (Zhang et al., 2011) show that the leading edge of the gas plume contains higher concentrations of CO_2. This chromatographic partitioning can be explained by the higher solubility of H2S in water and different characteristics close to the leading shock of displacement (F.M.Jr.Orr, 2007). This indicates that the inclusion of H_2S in the injection stream may reduce the storage capacity of the reservoir. Furthermore, Zaidin et al. (2024) investigate the effect of H_2S on CO_2 storage in saline aquifers. In their study they measure the solubility of H_2S-CO_2 mixtures and model the effect on CO_2 storage at the reservoir scale. Their findings indicate that H_2S has a negligible effect on CO_2 as in their model the amount of dissolved CO_2 decreases only slightly.

In this simulation, 5 mol% H_2S is co-injected with CO_2. The injection schedules per well are identical to the SPE11b benchmark but the total injection rate is reduced to 2800kgd^{-1}. In Fig. 10, the molar fraction of each component in the aqueous phase is shown at year 600. Evidently, the solution to the flow problem is

similar to that of the original SPE11b benchmark. However, the characteristic wavelength of the dissolution fingers is smaller in size.

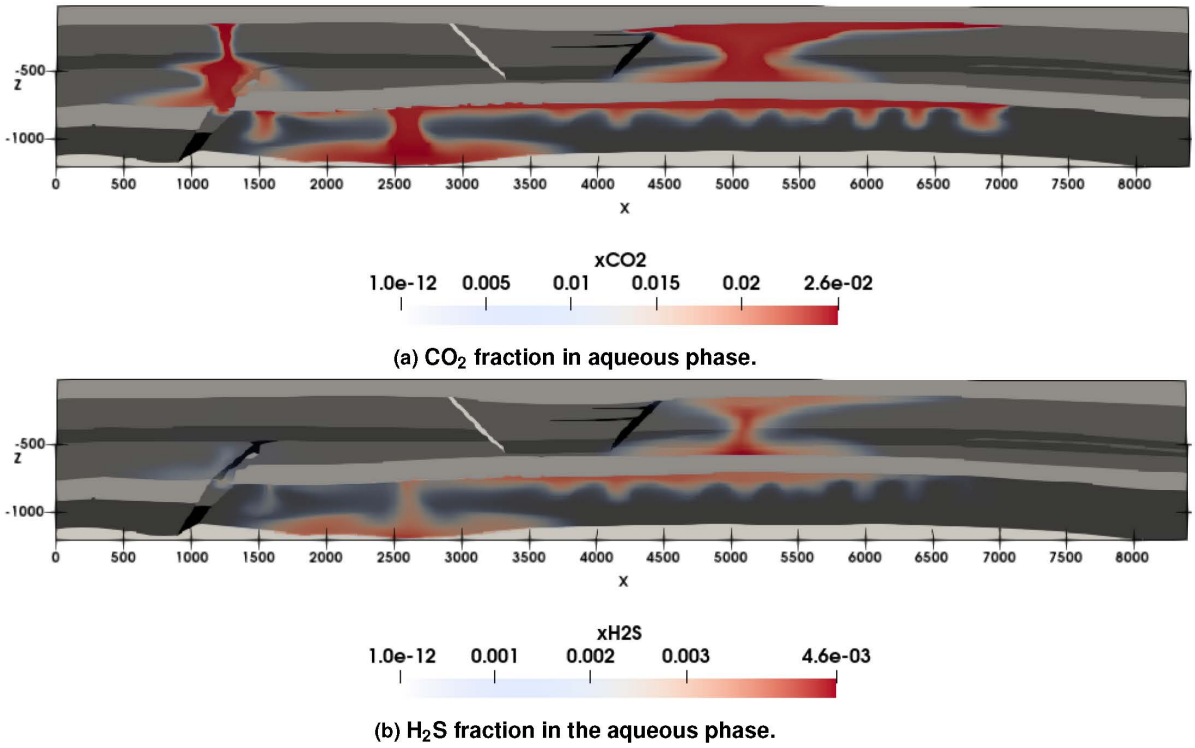

(a) CO_2 fraction in aqueous phase.

(b) H_2S fraction in the aqueous phase.

Figure 10—Simulation results of SPE11b with CO_2- H_2S coinjection in year 600.

Conclusion and recommendations

The solubility of CO_2 in aquifer water, the buoyancy of gaseous CO_2, diffusion and capillary forces are critical factors for accurate simulation of Geological Carbon Storage (GCS). In this study, the SPE11b and SPE11c benchmark models are simulated using the open-DARTS framework. In both models, CO_2 is effectively trapped under the capillary barriers, migrates across different units and dissolves into the aquifer brine. For the 11b model, a structured mesh is employed at various resolutions ranging from roughly 50K to 600K gridlocks. The results indicate that the solution for the SPE11b benchmark starts to converge at a vertical resolution of 1340 and horizontal resolution of 240 blocks per dimension, resulting in a 300K grid, with regards to dissolved mobile and immobile CO_2. However, the amount of CO_2 in the sealing units is found to be highly resolution-dependent, which we attribute to the use of a structured grid. Previous studies by Wapperom et al. (2024) clearly demonstrate that a similar reservoir structure is susceptible to grid-orientation effects.

The SPE11c benchmark model which is an extruded version of the SPE11b, is simulated with a grid resolution of about 8M active gridlocks. Comparison with the 2D simulation results of SPE11b reveals that this resolution is insufficient to produce an accurate solution. Generally, the SPE11 benchmark requires high-resolution and high-performance computing resources to obtain a converged solution due to a combination of many complex physical mechanisms.

One of the limitations of the SPE11 benchmark is the representation of the injection stream as pure CO_2. In real-life industrial applications, the stream of injected gas is expected to be a combination of CO_2 and various impurities depending on the source of CO_2. For this reason, the proposed benchmark is extended to include impurities in the injection stream and tested on the SPE11b structural model keeping most of the other parameters the same. In our simulation, H_2S was co-injected with CO_2 in the injection stream.

The results demonstrate chromatographic partitioning of the injected components which can be used for monitoring of CO_2 plum dynamics.

References

Bachu, S. and Bennion, D. B. (2009). Chromatographic partitioning of impurities contained in a co2 stream injected into a deep saline aquifer: Part 1. effects of gas composition and in situ conditions. *International Journal of Greenhouse Gas Control*, **3**(4):458–467.

Bando, S., Takemura, F., Nishio, M., Hihara, E., and Akai, M. (2004). Viscosity of Aqueous NaCl Solutions with Dissolved CO2 at (30 to 60) ◦ C and (10 to 20) MPa. *Journal of Chemical & Engineering Data*, **49**(5):1328–1332.

Eiken, O., Ringrose, P., Hermanrud, C., Nazarian, B., Torp, T. A., and Hoier, L. (2011). Lessons learned from 14 years of CCS operations: Sleipner, In Salah and Snohvit. *Energy Procedia*, **4**:5541–5548.

Elenius, M., Voskov, D., and Tchelepi, H. (2015). Interactions between gravity currents and convective dissolution. *Advances in WaterResources*, **83**:77–88.

Fenghour, A., Wakeham, W. A., and Vesovic, V. (1998). The Viscosity of Carbon Dioxide. *Journal ofPhysical and Chemical Reference Data*, **27**(1):31–44.

Flemisch, B., Nordbotten, J. M., Ferno, M., Juanes, R., Both, J. W., Class, H., Delshad, M., Doster, F., Ennis-King, J., Franc, J., Geiger, S., Glaser, D., Green, C., Gunning, J., Hajibeygi, H., Jackson, S. J., Jammoul, M., Karra, S., Li, J., Matthai, S. K., Miller, T., Shao, Q., Spurin, C., Stauffer, P., Tchelepi, H., Tian, X., Viswanathan, H., Voskov, D., Wang, Y., Wapperom, M., Wheeler, M. F., Wilkins, A., Youssef, A. A., and Zhang, Z. (2024). The FluidFlower Validation Benchmark Study for the Storage ofCO2. *Transport in Porous Media*, **151**(5):865–912.

F.M. Orr Jr. (2007). Theory ofGas Injection Processes. Tie-Line Publications, ISBN - 87-989961-2-5.

Garcia, J. E. (2001). Density of aqueous solutions of CO2. Technical report, Lawrence Berkeley National Laboratory (LBNL), Berkeley, CA.

Hnedkovsky, L., Wood, R., and Majar, V. (1996). Volumes ofaqueous solutions ofCH4, CO2, H2S andNH3 at temperatures from 298.15 K to 705 K and pressures to 35 MPa. *The Journal of Chemical Thermodynamics*, **28**(2):125–142.

Islam, A. W. and Carlson, E. S. (2012). Viscosity Models and Effects of Dissolved CO2. *Energy & Fuels*, **26**(8):5330–5336.

Khait, M. and Voskov, D. (2021). A gpu-based integrated simulation framework for modelling of complex subsurface applications. In Society of Petroleum Engineers - SPE Reservoir Simulation Conference 2021, RSC 2021.

Khait, M. and Voskov, D. V. (2017). Operator-based linearization for general purpose reservoir simulation. *Journal of Petroleum Science and Engineering*, **157**:990–998.

Koschel, D., Coxam, J.-Y., Rodier, L., and Majer, V. (2006). Enthalpy and solubility data of CO2 in water and NaCl(aq) at conditions of interest for geological sequestration. *Fluid Phase Equilibria*, **247**(1-2):107–120.

Krevor, S., Blunt, M. J., Benson, S. M., Pentland, C. H., Reynolds, C., Al-Menhali, A., and Niu, B. (2015). Capillary trapping for geologic carbon dioxide storage - From pore scale physics to field scale implications. *International Journal of Greenhouse Gas Control*, **40**:221–237.

Lemmon, E., Bell, I., Huber, M., and McLinden, M. (2023). Thermophysical properties of fluid systems. *Technical report*, The National Institute of Standards and Technology (NIST).

Lyu, X., Khait, M., and Voskov, D. (2021). Operator-Based Linearization Approach for Modeling of Multiphase Flow with Buoyancy and Capillarity. *SPE Journal*, **26**(04):1858–1875.

Lyu, X. and Voskov, D. (2023). Advanced modeling of enhanced co2 dissolution trapping in saline aquifers. *International Journal of Greenhouse Gas Control*, 127.

Metz, B., Davidson, O., de Coninck, H., Loos, M., and Meyer, L. (2005). IPCC Special Report on Carbon dioxide Capture and Storage. *Policy Stud*.

Michelsen, M. L. (1982). The isothermal flash problem. Part II. Phase split calculation. *Fluid Phase Equilibria*, **9**:21–40.

Neufeld, J. A., Hesse, M. A., Riaz, A., Hallworth, M. A., Tchelepi, H. A., and Huppert, H. E. (2010). Convective dissolution of carbon dioxide in saline aquifers. *Geophysical research letters*, **37**(22).

Nordbotten, J. M., Ferno, M., Flemisch, B., Juanes, R., and Jorgensen, M. (2022). Final Benchmark Description: Fluid-Flower International Benchmark Study.

Nordbotten, J. M., Ferno, M. A., Flemisch, B., Kovscek, A. R., and Lie, K.-A. (2024). The 11th Society of Petroleum Engineers Comparative Solution Project: Problem Definition. *SPE Journal*, **29**(05):2507–2524.

Pau, G. S., Bell, J. B., Pruess, K., Almgren, A. S., Lijewski, M. J., and Zhang, K. (2010). High-resolution simulation and characterization of density-driven flow in CO2 storage in saline aquifers. *Advances in Water Resources*, **33**(4):443–455.

Peng, D.-Y. and Robinson, D. B. (1976). A New Two-Constant Equation of State. *Industrial & Engineering Chemistry Fundamentals*, **15**(1):59–64.

Pruess, K., García, J., Kovscek, T., Oldenburg, C., Rutqvist, J., Steefel, C., and Xu, T. (2004). Code intercomparison builds confidence in numerical simulation models for geologic disposal ofCO2. *Energy*, **29**(9-10):1431–1444.

Pruess, K. and Nordbotten, J. (2011). Numerical Simulation Studies of the Long-term Evolution of a CO2 Plume in a Saline Aquifer with a Sloping Caprock. *Transport in Porous Media*, **90**(1):135–151.

Riaz, A., Hesse, M., Tchelepi, H. A., and Orr, F. M. (2006). Onset of convection in a gravitationally unstable diffusive boundary layer in porous media. *Journal of Fluid Mechanics*, **548**(-1):87.

Ringrose, P. (2020). How to Store CO2 Underground: Insights from early-mover CCS Projects. Springer International Publishing, Cham.

Savary, V., Berger, G., Dubois, M., Lacharpagne, J.-C., Pages, A., Thibeau, S., and Lescanne, M. (2012). The solubility of co2+h2s mixtures in water and 2m nacl at 120°c and pressures up to 35mpa. *International Journal of Greenhouse Gas Control*, **10**:123–133.

Spycher, N., Pruess, K., and Ennis-King, J. (2003). CO2-H2O mixtures in the geological sequestration of CO2. I. Assessment and calculation of mutual solubilities from 12 to 100 C and up to 600 bar. *Geochimica et Cosmochimica Acta*, **67**(16):3015–3031.

Tian, X., Wapperom, M., Gunning, J., Jackson, S., Wilkins, A., Green, C., Ennis-King, J., and Voskov, D. (2024). A history matching study for the fluidflower benchmark project. *Transport in Porous Media*, **151**(5):1113–1139.

Voskov, D., Saifullin, I., Novikov, A., Wapperom, M., Orozco, L., Seabra, G. S., Chen, Y., Khait, M., Lyu, X., Tian, X., de Hoop, S., and Palha, A. (2024). Open Delft Advanced Research Terra Simulator (open-DARTS). *Journal of Open Source Software*, **9**(99):6737.

Voskov, D. V. (2017). Operator-based linearization approach for modeling of multiphase multi-component flow in porous media. *Journal of Computational Physics*, **337**:275–288.

Wapperom, M., dos Santos Heringer, J., Nichita, D., and Voskov, D. (2025). A hybrid-EoS approach for multiphase equilibrium calculations of reservoir mixtures with brine. *Manuscript submitted for publication*.

Wapperom, M., Tian, X., Novikov, A., and Voskov, D. (2024). FluidFlower Benchmark: Lessons Learned from the Perspective of Subsurface Simulation. *Transport in Porous Media*, **151**(5):1033–1052.

Whitson, C. H. and Michelsen, M. L. (1989). The negative flash. *Fluid Phase Equilibria*, **53**:51–71.

Whittaker, S., Rostron, B., Khan, D., Hajnal, Z., Qing, H., Penner, L., Maathuis, H., and Goussev, S. (2004). IEA GHG Wey- burn CO2 monitoring and storage project summary report 2000-2004. Proceedings of the 7th International Conference on Greenhouse Gas Control Technologies, pages 15–72.

Zaidin, M., Valtz, A., Chapoy, A., and Tewari, R. (2024). Exploring co2-h2s storage in deep saline aquifers: A case study from an offshore gas field in malaysia. from lab to numerical simulation. IPTC International Petroleum Technology Conference, All Days:IPTC-23428-EA.

Zhang, W., Xu, T., and Li, Y. (2011). Modelingoffateandtransportofcoinjectionofh2s withco2 indeep saline formations. *Journal of Geophysical Research: Solid Earth*, **116**(B2).

Ziabakhsh-Ganji, Z. and Kooi, H. (2012). An Equation ofState for thermodynamic equilibrium of gas mixtures and brines to allow simulation ofthe effects ofimpurities in subsurface CO2 storage. *International Journal of Greenhouse Gas Control*, **11**:S21–S34.